Ground-based full-sky imaging polarimetry of rapidly changing skies and its use for polarimetric cloud detection

Gábor Horváth, András Barta, József Gál, Bence Suhai, and Ottó Haiman

For elimination of the shortcomings of imaging polarimeters that take the necessary three pictures sequentially through linear-polarization filters, a three-lens, three-camera, full-sky imaging polarimeter was designed that takes the required pictures simultaneously. With this polarimeter, celestial polarization patterns can be measured even if rapid temporal changes occur in the sky: under cloudy sky conditions, or immediately after sunrise or prior to sunset. One of the possible applications of our polarimeter is the ground-based detection of clouds. With use of the additional information of the degree and the angle of polarization patterns of cloudy skies measured in the red (650 nm), green (550 nm), and blue (450 nm) spectral ranges, improved algorithms of radiometric cloud detection can be offered. We present a combined radiometric and polarimetric algorithm that performs the detection of clouds more efficiently and reliably as compared with an exclusively radiometric cloud-detection algorithm. The advantages and the limits of three-lens, three-camera, full-sky imaging polarimeters as well as the possibilities of improving our polarimetric cloud detection method are discussed briefly. © 2002 Optical Society of America

OCIS codes: 010.3920, 100.0100, 120.5410, 260.5430, 280.0280, 290.1310.

1. Introduction

To our knowledge, in the past, three 180° field-of-view imaging polarimeters have been designed for the measurement of the distribution of the degree and the angle of linear polarization in the full sky.[1–8] All of these polarimeters take three pictures of the entire sky through linear polarization filters with different directions of the preferred transmission axis. The patterns of the degree and the angle of polarization of skylight are determined with use of computer evaluation of these three pictures.

North and Duggin[1] obtained partial Stokes vectors and derivative images of the firmament by taking advantage of a four-lens photographic camera. Although the spherical convex mirror of their imaging polarimeter encompasses a field of view of almost 180°, the instrument cannot record data of the entire sky dome, since the camera of the researchers' equip-

ment is set up on a large, heavy tetrapod at a height of several meters above the mirror placed on the ground, so the tetrapod as well as the camera screen out certain areas of the firmament. Furthermore, the equipment is rather voluminous and cumbersome. This fact does not permit easy and rapid setup, disassembly, transfer, and transport. The main advantage of this polarimeter is that it takes all needed polarization pictures of the sky simultaneously with use of all four lenses of the camera.

The setup of the full-sky imaging polarimeter of Voss and Liu[2] and Liu and Voss[3] with use of a 180° fish-eye lens is much easier. This equipment is also not portable, because it needs a mains power supply and connection with a computer; furthermore, its CCD image sensor has to be thermoelectrically cooled ($-40\ °C \leq T \leq -30\ °C$). This polarimeter can, however, be made more portable with a rectifier battery combination. Since a wide sun occulter is used, this instrument cannot measure the part of the sky in which the Babinet and Brewster points occur. The overall time needed for one complete measurement with this polarimeter is 1.5–2 min in normal daylight.

The full-sky imaging polarimeter designed by Gál *et al.*[4–6] and Pomozi *et al.*[7,8] is portable and easy to handle and set up. Its main component is a roll-film

The authors are with Eötvös University, Department of Biological Physics, H-1117 Budapest, Pázmány Sétány 1, Hungary. G. Horvath can be reached at gh@arago.elte.hu.

photographic camera set up on a tripod and equipped with a 180° fish-eye lens, including a built-in rotating disc (filter wheel) that carries three neutral density linear polarization filters of different orientation of the preferred transmission axis. This polarimeter, using photoemulsion as a detector and a scanner as a digitizer of its analog data, has a more limited dynamic range than a polarimeter that uses a CCD array.[2,3] Under normal illumination conditions of the sunlit day sky, the overall time needed for one complete measurement with this polarimeter is 6–8 sec.

The major shortcoming of the polarimeters of Voss and Liu[2], Liu and Voss[3], Gál *et al.*,[4–6] and Pomozi *et al.*[7,8] is their slowness, owing to the fact that they record the three polarization pictures of the full sky sequentially. One cycle of three exposures and–in between–the exchange of the polarizer may well take several seconds or minutes, depending on the time of exposure. Thus these instruments cannot be used if the cycle duration is comparable with the time, during which the optical characteristics of the sky change considerably. Such situations occur (i) if the sky is cloudy and the clouds move fast, (ii) when moving aerial objects (e.g., birds or airplanes) occur in the firmament, (iii) immediately after sunset or prior to sunrise, when the radiance of skylight changes rapidly and, moreover, the time of exposure increases considerably owing to the relatively low radiance of the sky, or (iv) the platform of the polarimeter is moving or rocking (being on the board of a ship, for example).

To eliminate the major shortcoming of the above-mentioned polarimeters, we designed a three-lens, three-camera, full-sky imaging polarimeter that takes the three polarization pictures of the entire sky simultaneously rather than sequentially. Thus celestial polarization patterns can be recorded even if rapid temporal changes occur in the sky: under cloudy sky conditions, or immediately after sunrise and prior to sunset. In our present paper, we first describe briefly our instrument.

One of the possible applications of our polarimeter is the ground-based detection of clouds. In many meteorological stations, the accurate determination of sky conditions, especially the detection of clouds, is a desirable yet rarely attainable goal. Traditionally, sky conditions are reported by human observers with considerable discrepancies between individual subjective reports. In practice, employing human observers is not always feasible, owing to budgetary constraints. Human observers can be replaced by automatic full-sky imager systems, like the Scripps-produced Whole Sky Imager, or the TSI-880 Total Sky Imager produced by the Yankee Environmental Systems, Inc.[9] These systems provide real-time processing and display of daytime sky conditions with use of common embedded image-processing algorithms that detect the clouds radiometrically by filtering the color picture of the sky so that the approximate value of the cloud-cover fraction can be calculated.

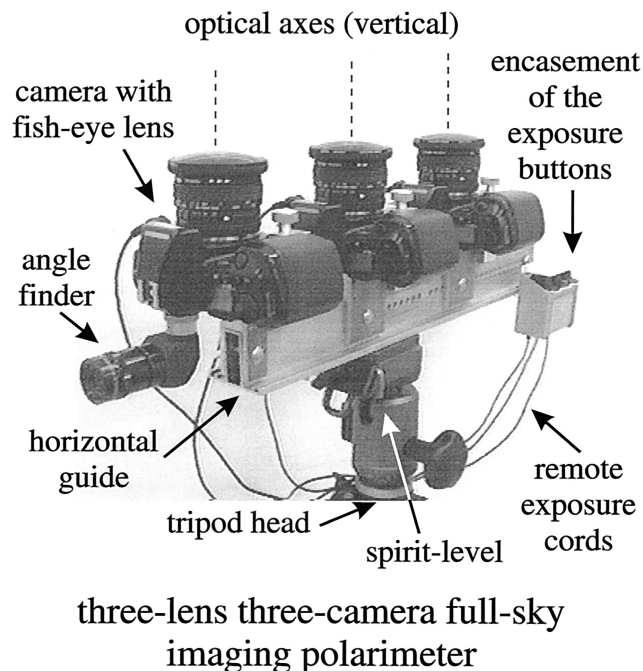three-lens three-camera full-sky imaging polarimeter

Fig. 1. Setup of our three-lens, three-camera, full-sky (180° field-of-view) imaging polarimeter.

With use of the additional information obtained through evaluation of both the degree and the angle of polarization patterns of cloudy skies that are measured by our full-sky imaging polarimeter in the red (650 nm), green (550 nm), and blue (450 nm) spectral ranges, the algorithms of radiometric cloud detection[9–12] can be improved significantly. Accordingly, the second aim of this paper is to present an efficient combined radiometric and polarimetric algorithm that detects clouds more efficiently and reliably as compared with an exclusively radiometric cloud-detection algorithm. Finally, the advantages and limits of three-lens, three-camera, full-sky imaging polarimeters as well as the possibilities of improving our polarimetric cloud-detection method are briefly discussed.

2. Materials and Methods

A. Three-Lens, Three-Camera, Full-Sky Imaging Polarimeter

The setup of our three-lens, three-camera, full-sky imaging polarimeter is shown in Figs. 1–4. The polarimeter is composed of three Nikon F801 roll-film photographic cameras (Fig. 1), each equipped with a Sigma fish-eye lens (Fig. 2). The F-number of the lenses is 4, their focal length is 8 mm, and their field of view is 180°. The cameras are fixed on a tripod parallel to each other onto a horizontal guide pointing always northward during the measurement (Fig. 3) with the optical axes of the fish-eye lenses vertical, pointing toward the zenith. On one of the outside cameras the vertical direction through the view finder is turned to horizontal by means of a 90° angle finder. The simultaneous triggering of all three
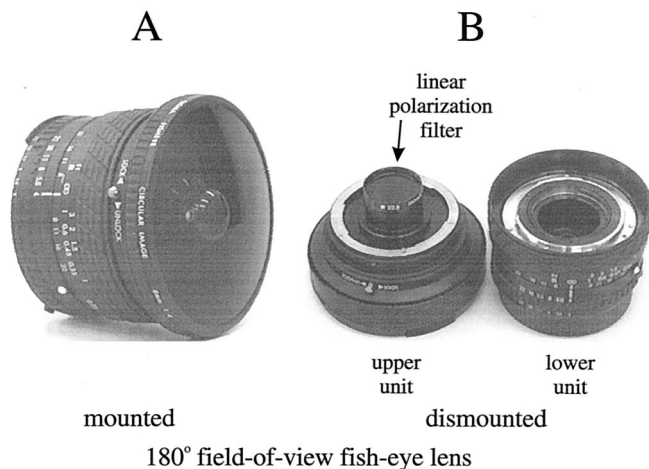
Fig. 2. Sigma fish-eye lens in the mounted (a) and dismounted (b) state used in our polarimeter.

Fig. 4. Blocking of the direct solar radiation by a sun occulter held by an assistant to eliminate multiple internal reflections at the refracting surfaces within the fish-eye lenses of our polarimeter.

cameras is mechanically ensured by the synchronous pressing of the buttons of the remote exposure cords. The same values of aperture and exposure are set manually on all three cameras, which are focused to infinity. Obviously, the distance of approximately 10 cm between the neighboring cameras does not result in a disparity (or parallax) error.

Each Sigma fish-eye lens used [Fig. 2(a)] is composed of two (upper and lower) lens groups (optical units) with a circular filter mount in between [Fig. 2(b)]. Into the mounts neutral density linear polarization filters are inserted in such a way that the angles β between their preferred transmission axes and the horizontal guide pointing northward are 0°, 60°, and 120° in the first, second, and third cameras, respectively (Fig. 3). Broadband (275–750 nm) linear polarizers (typename HNP'B, Polaroid Europe Ltd., London, England, http://www.polaroid.com[13]) were chosen. The use of three linear polarizers did not affect the accuracy of the measurements, because the small (22.5-mm diameter) circular filters were cut out from neighboring areas of the same filter sheet, the high optical quality and homogeneity of which was guaranteed by the manufacturer. Thus all three filters possessed the same optical characteristics.

The type and sensitivity of film material used as a detector depends on the type of recording. For daylight photography we used Fujichrome Sensia II 100 or 200 ASA color reversal film; the maxima and half-
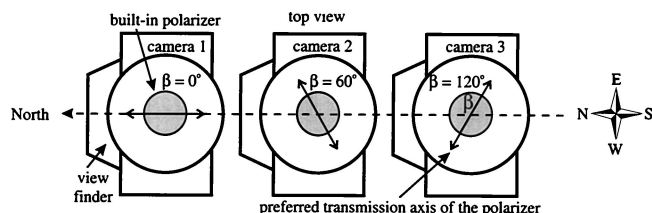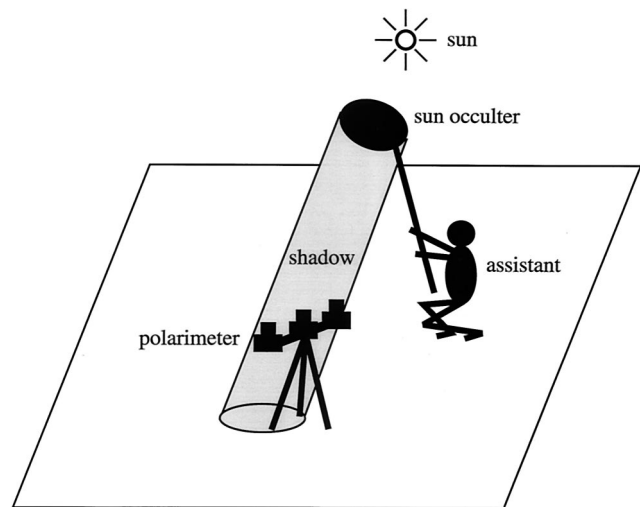

Fig. 3. Direction of the preferred transmission axis of the built-in linear polarization filters in our polarimeter.

bandwidths of its spectral sensitivity curves are $\lambda_{red} = 650 \pm 30$ nm, $\lambda_{green} = 550 \pm 30$ nm, and $\lambda_{blue} = 450 \pm 50$ nm. To minimize ghost effects owing to internal reflections of direct sunlight from the refracting surfaces within the fish-eye lenses and the blooming effect caused by the direct solar radiation and the limited dynamic range of the photoemulsion, the direct sunlight was screened out. A sun occulter was fixed to a rod held by an assistant (Fig. 4) and positioned at a distance as great as possible from the polarimeter to minimize the area of its shadow on the picture of the sky dome to be photographed (Fig. 5).

B. Evaluation of the Three Polarization Pictures of the Sky

The evaluation method of the three polarization pictures taken with our three-lens, three-camera, full-sky imaging polarimeter is the same as in the case of our one-lens, one-camera, full-sky imaging polarimeter published previously[4–8] and similar to the method of Voss and Liu[2] and Liu and Voss.[3] We have to add here only that the reliability and repeatability of the development of the color reversal films was ensured through the development of all films in the same professional photographic laboratory (in Budapest) with use of the same automatically controlled process. To minimize the possible slight differences between the photoemulsions, we took the three roll films used in a given measurement from the same lot furnished by the manufacturer. The developed three color pictures of a given sky taken with the three different alignments (β = 0°, 60°, 120°) of the linear polarizer are digitized in 3×8-bit (R, G, B; true color) with use of a Hewlett-Packard ScanJet 6100C, which performs concurrently their quantitative evaluation (pixelwise determination of the numerical value of the radiance I as well as the degree p and angle α of polarization). This is done with use of a digital image-processing program provided with
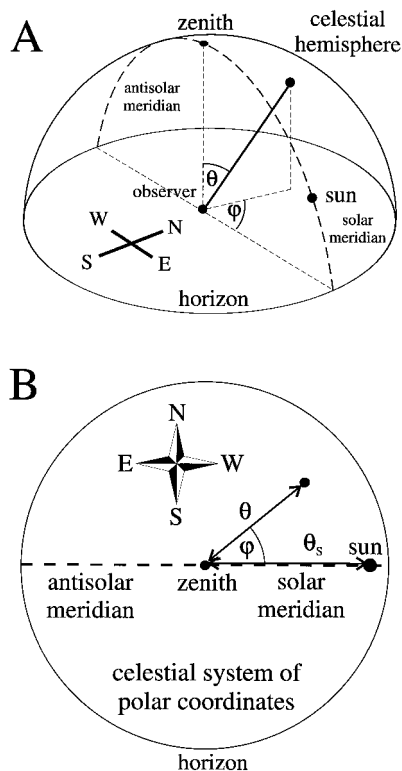
Fig. 5. (a) Three-dimensional celestial polar coordinate system. (b) Two-dimensional celestial system of polar coordinates used in the circular sky photographs. East is on the left (rather than on the right) of the compass rose because the view is up through the celestial dome rather than down onto a map.

the scanner for the three spectral ranges, namely the red (650 nm), green (550 nm), and blue (450 nm), in which the three color-sensitive layers of the used photoemulsion have the maximal sensitivity. The ultimate results are p and α maps that show the patterns of the degree and the angle of polarization of skylight in the three (r, g, b) spectral channels. Note that for all three channels, visualization by the same high-resolution gray-coding of the maps is used.

The calibration of our system involved the determination of the influence of the fish-eye lens on the ray optical parameters of the light that passes through it and the determination of the transfer function of the evaluation process, that is, the relation between the incident radiance and the corresponding digital value obtained by the digitization process (instrument output). Since the radiometric calibration of our system without polarization is the same as in the case of our system with use of a one-lens, one-camera, full-sky imaging polarimeter described previously,[4–8] we describe here briefly only the characterization of our Sigma fish-eye lenses (being the only new elements in our system) in Mueller matrix representation.

Focused at infinity, our 180° field of view fish-eye lenses form circular images with a radius of $R = 10$ mm in their focal planes (on the photoemulsion). Rays incident with a given off-axis angle θ_o are focused onto a circle of radius $r(\theta_o)$ [inset in Fig. 6(a)].
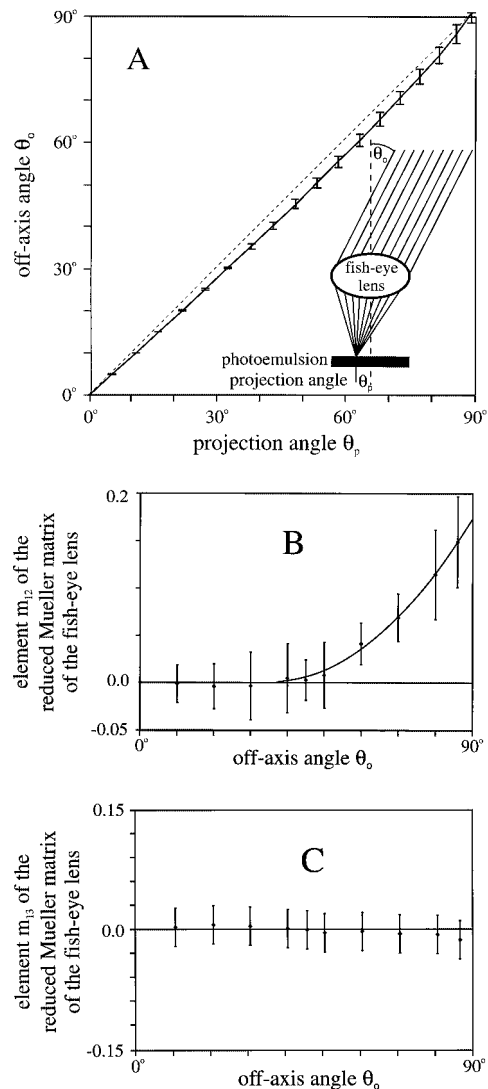

Fig. 6. (a) Relationship between the projection angle θ_p (projected onto the photoemulsion by the fish-eye lens) and the off-axis angle θ_o. The broken line represents the ideal case when $\theta_p = \theta_o$. (b, c) Change of the elements m_{12} and m_{13} of the reduced Mueller matrix of the fish-eye lens without polarizer as a function of θ_o.

Let us introduce the projection angle by the formula $\theta_p = 90° \times r/R$. To determine the angular transfer function $\theta_p(\theta_o)$ of the camera/fish-eye lens system, a camera with a fish-eye lens was placed in the center of an arc carrying black-and-white stripes $\Delta\theta_o = 5°$ apart that were photographed. On the image (diameter $2R$), r/R values were determined, yielding the θ_p projections that were to be correlated with the θ_o values. The measured inverse angular transfer function $\theta_o(\theta_p)$ is shown in Fig. 6(a). In all of the circular images (photographs as well as p and α patterns) of Figs. 5(b), 7–12 the center is the zenith, and the zenith angle $\theta = \theta_o(\theta_p)$ is directly proportional to the radius from the center. The fish-eye lens rolloff was calculated as described previously[5]; it was modeled rather than measured, because we were interested in polarization properties; thus the rolloff is not that important.
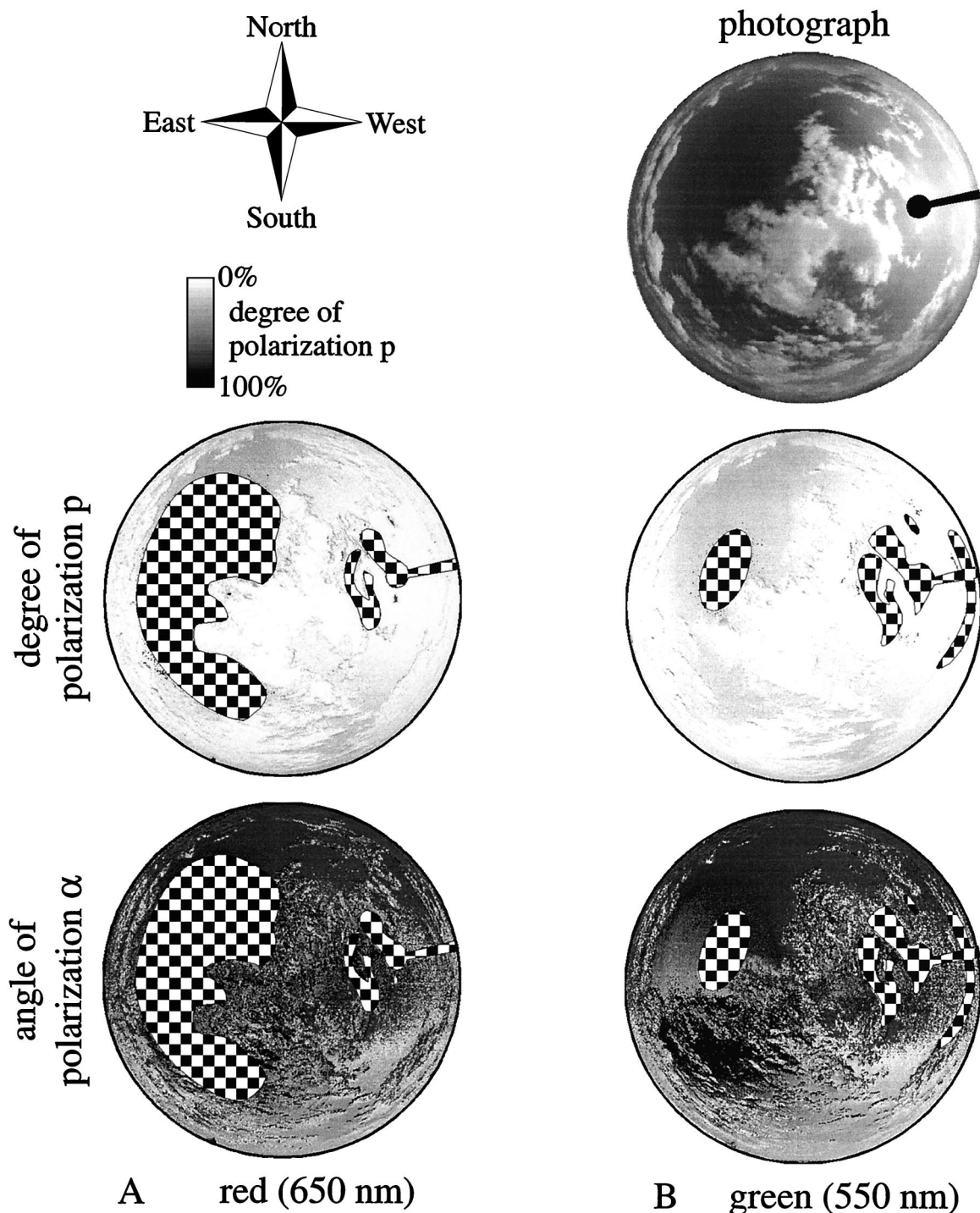
Fig. 7. Photograph and the patterns of the degree of linear polarization p and angle of polarization α of a sky with fast-moving cumuli measured by our three-lens, three-camera, full-sky imaging polarimeter in simultaneous mode in the red (650 nm), green (550 nm), and blue (450 nm) spectral ranges at Kunfehértó (46° 23′ N, 19° 24′ E, Hungary) on 15 August 2000 at 17:00 (local summer time = UTC + 2). The overexposed regions of the sky around the sun and the underexposed regions of the sky at about 90° from the sun as well as the sun occulter are checkered in the p and α patterns.

To determine the change of the optical properties of the light passing through the fish-eye lens without polarization filter, we have to know its Mueller matrix $M(\theta_o)$ as a function of the off-axis angle θ_o. In general, this means that we have to know the functions of its 16 elements: $M_{11}(\theta_o)$, $M_{12}(\theta_o)$, ..., $M_{44}(\theta_o)$. However, in the case of our full-sky imaging polarimeter we do not need all of these elements because of the following reasons[2]: (i) Since the photoemulsion senses only the intensity of the incoming light, only the first row (M_{11}, M_{12}, M_{13}, M_{14}) of the fish-eye lens Mueller matrix must be determined.
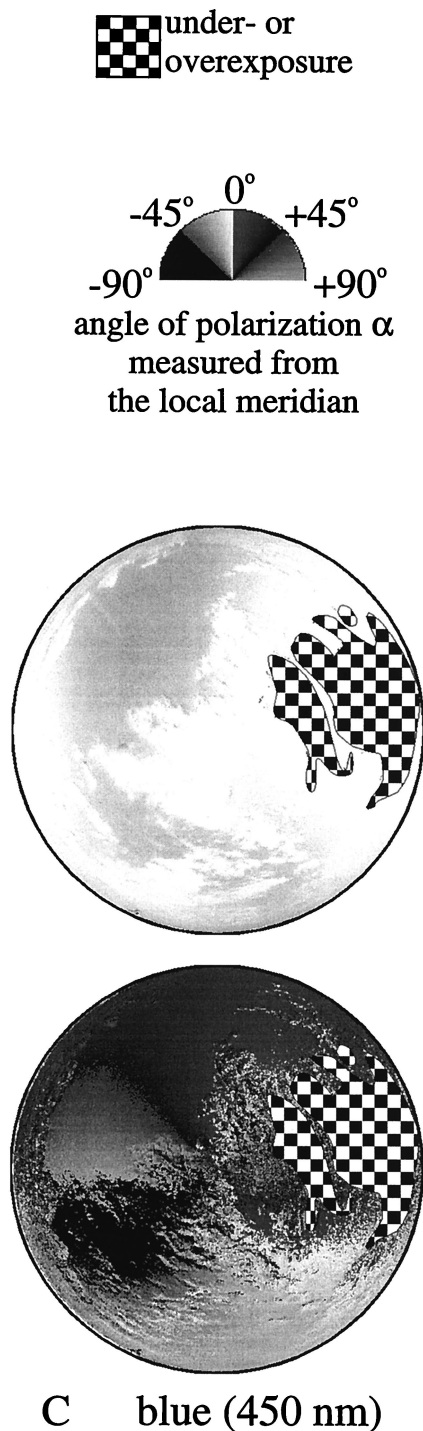
under- or overexposure

$$-45° \quad 0° \quad +45°$$
$$-90° \quad +90°$$

angle of polarization α
measured from
the local meridian

North
East — West
South

0%
degree of
polarization p
100%

degree of polarization p

angle of polarization α

C   blue (450 nm)

A   red (650 nm)

Fig. 7. Continued.

Fig. 8. Same as Fig. 7 for a clear, cloudless sky with the same solar position at Kunfehértó (46° 23′ N, 19° 24′ E, Hungary) on 17 August 2000 at 17:00 (local summer time = UTC + 2).

(ii) In general, the light in the atmosphere is not circularly polarized,[14,15] so we do not need to perform the pertaining measurements. (iii) Following the calibration method of Voss and Liu,[2] we used the reduced Mueller matrix m, which is the fish-eye lens Mueller matrix normalized to M_{11} ($m_{ij} = M_{ij}/M_{11}$).

Consequently, it was enough to determine only the spectral and spatial characteristics of the elements $m_{12}(\theta_o)$ and $m_{13}(\theta_o)$ of the reduced Mueller matrix of the fish-eye lens. Experimentally we found that $m_{12}(\theta_o)$ and $m_{13}(\theta_o)$ were rotationally symmetric around the optical axis and independent of wavelength for all three Sigma fish-eye lenses that were used. The measured elements $m_{12}(\theta_o)$ and $m_{13}(\theta_o)$ of the reduced Mueller matrix are seen in Figs. 6(b) and 6(c) which were the same for all three fish-eye lenses.

photograph

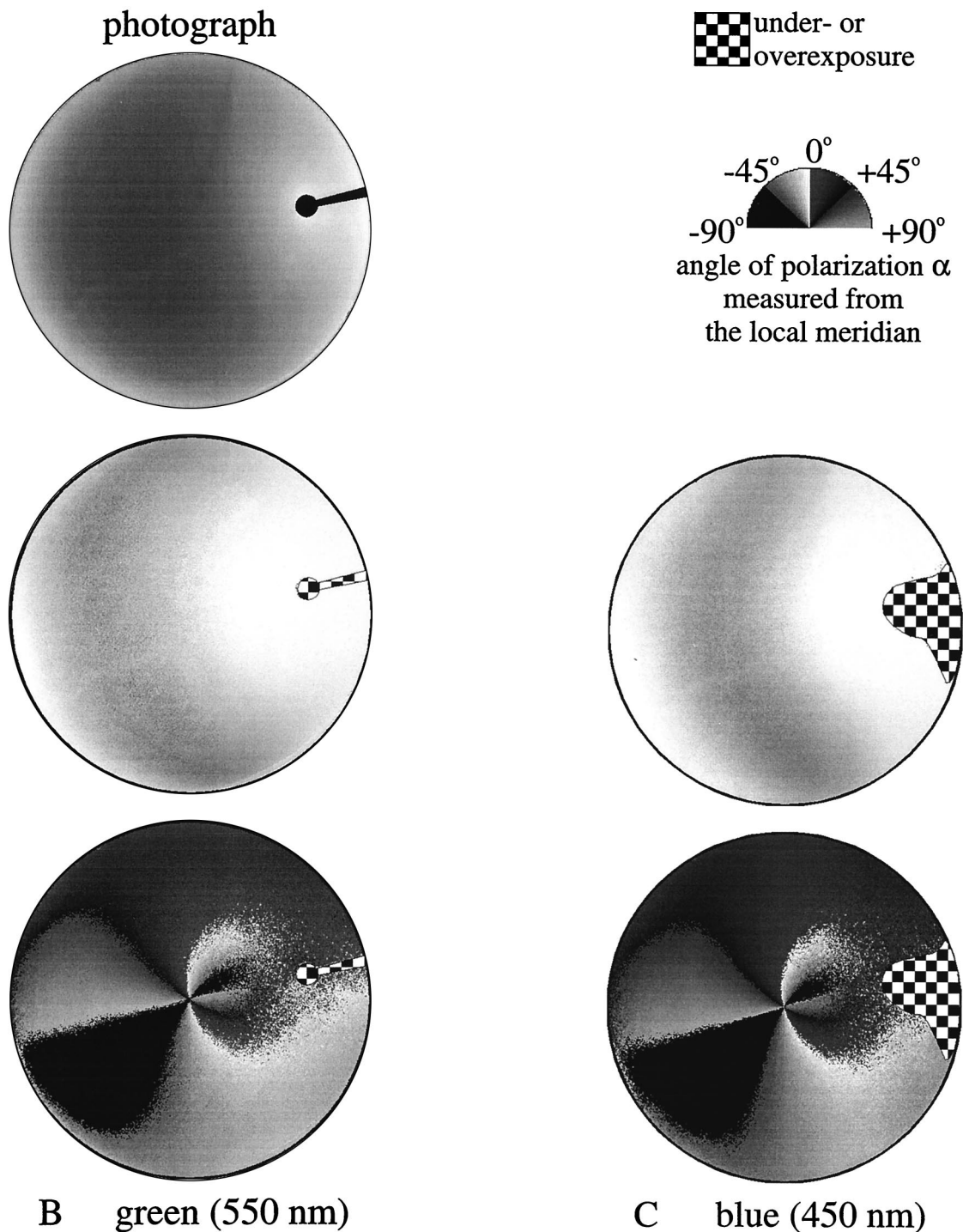B green (550 nm)

C blue (450 nm)

Fig. 8. Continued.

The Mueller matrix $M_p(q_1, q_2, \beta)$ of the linear polarizer in the fish-eye lenses was calculated on the basis of the formula given by Voss and Liu[2] [Eq. (14)], where q_1 and q_2 are the transmittances of the polarizer along the preferred axis and an axis 90° to this axis, β is the angle between the polarizer-preferred transmittance plane and a reference plane (β was 0°, 60°, and 120° in the first, second, and third cameras, respectively; Fig. 3). The values of $q_1(\lambda)$ and $q_2(\lambda)$ of

the HNP'B linear polarizers for different wavelengths λ were obtained from the catalog of the manufacturer.[13] The total system Mueller matrix was computed as the product of the polarizer Mueller matrix and the fish-eye lens reduced Mueller matrix.

C. Algorithmic Detection of Clouds

After the digitization, processing, and evaluation of the three polarization pictures of a given sky taken
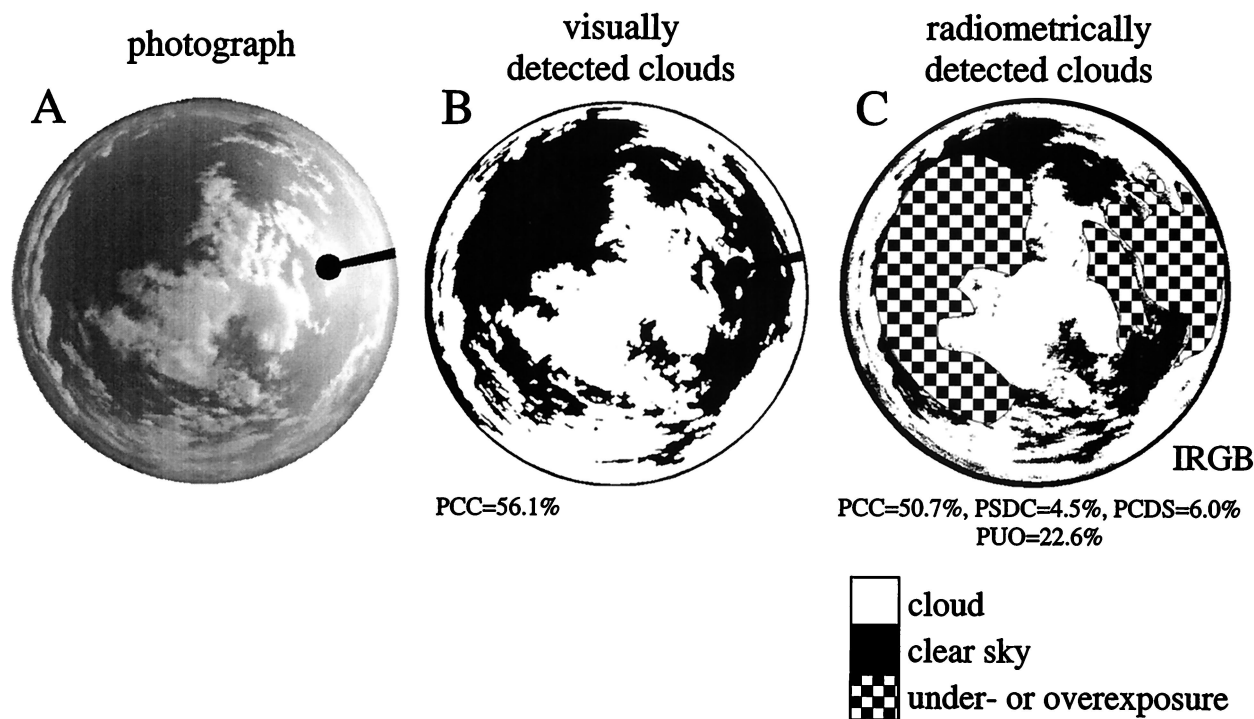
Fig. 9. (a) Photograph (identical with that in the first row of Fig. 7) of the partially cloudy sky, the polarization characteristics of which are shown in Fig. 7. (b) Cloudy (white) and clear (black) sky regions detected visually by the naked eye in (a). (c) Clouds detected radiometrically, where the under- or overexposed celestial areas are checkered as the sun occulter. PCC, proportion of cloud cover determined by the different detectors IRGB, PR, PG, PB, αR, αG, and αB; PSDC, proportion of (clear) sky detected (erroneously) as cloud; PCDS, proportion of clouds detected (erroneously) as (clear) sky; PUO, proportion of under- and/or overexposure.

with our full-sky imaging polarimeter, we obtain the values of nine optical variables for every pixel of the sky image: I_r, I_g, I_b, p_r, p_g, p_b, α_r, α_g, and α_b, that is, radiance I, degree of linear polarization p, and angle of polarization α measured in the red (r, 650 nm), green (g, 550 nm) and blue (b, 450 nm) spectral ranges. The essence of our cloud-detection algorithm is that for every pixel of the sky picture we make seven decisions: (1) Analyzing the values of I_r, I_g, and I_b, we determine the color of the pixel and decide if the pixel may belong to a colorless cloud or to a blue sky region. (2)–(7) Using the values of p_r, p_g, p_b, α_r, α_g, or α_b, we again decide if the pixel may be part of a cloud or a clear sky region.

Every decision is the outcome of its specific subalgorithm, called "detector." Detector (1) is symbolized by the letters IRGB, referring to the fact that it uses the I values measured in the R, G, B spectral ranges. Detectors (2)–(7) are symbolized by letters PR, PG, PB, αR, αG, and αB, because they use the measured values of p_r, p_g, p_b, α_r, α_g, or α_b, respectively. If detector IRGB identifies a pixel as "cloud," the pixel qualification is weighted by 3, because the decision relies on the use of three input data. The total weight of a pixel qualification is i, if it is identified as "cloud" by i detectors among detectors PR, PG, PB, αR, αG, αB (these six detectors make their decisions with use of one input datum each). The partial weight is 0 in every case in which the pixel is identified as "clear sky" by a given detector.

If the investigated pixel is under- or overexposed at least in one of the R, G, B spectral ranges, detector IRGB is inactive, resulting in a 0 partial weight value. Similarly, any other detector is inactive if the pixel is under- or overexposed in the corresponding spectral range (in the case of detectors PR or αG, for instance, in the R or G range of the spectrum, respectively). Let the number of active detectors be m. The partial weights are summed up, thus finally the investigated pixel has a total weight n ranging from 0 to 9 and coded by different grey shades (Figs. 11 and 12). n denotes how many times the pixel was identified as "cloud"; n is called the "number of cloud identification." At a given value of m, number n is proportional to the likelihood of cloud: the higher n is, the greater the probability is that the pixel belongs to a cloud in the picture. The authenticity (or reliability) of n is proportional to the number m of active detectors. The distributions of the n- and m-values in the sky are represented by gray-coded maps (Figs. 11 and 12). The functioning of the above-mentioned seven different detectors (subalgorithms) is described in the following subsections.

In the case of radiometric cloud detection only detector IRGB is used. Polarimetric cloud detection uses only detectors PR, PG, PB, αR, αG, and αB. We speak about combined (radiometric and polarimetric) cloud detection if all seven detectors are used. As we see below, the combined cloud-detection algorithm has seven control parameters: c, $p_0(Q)$, and $\Delta\alpha(Q)$,
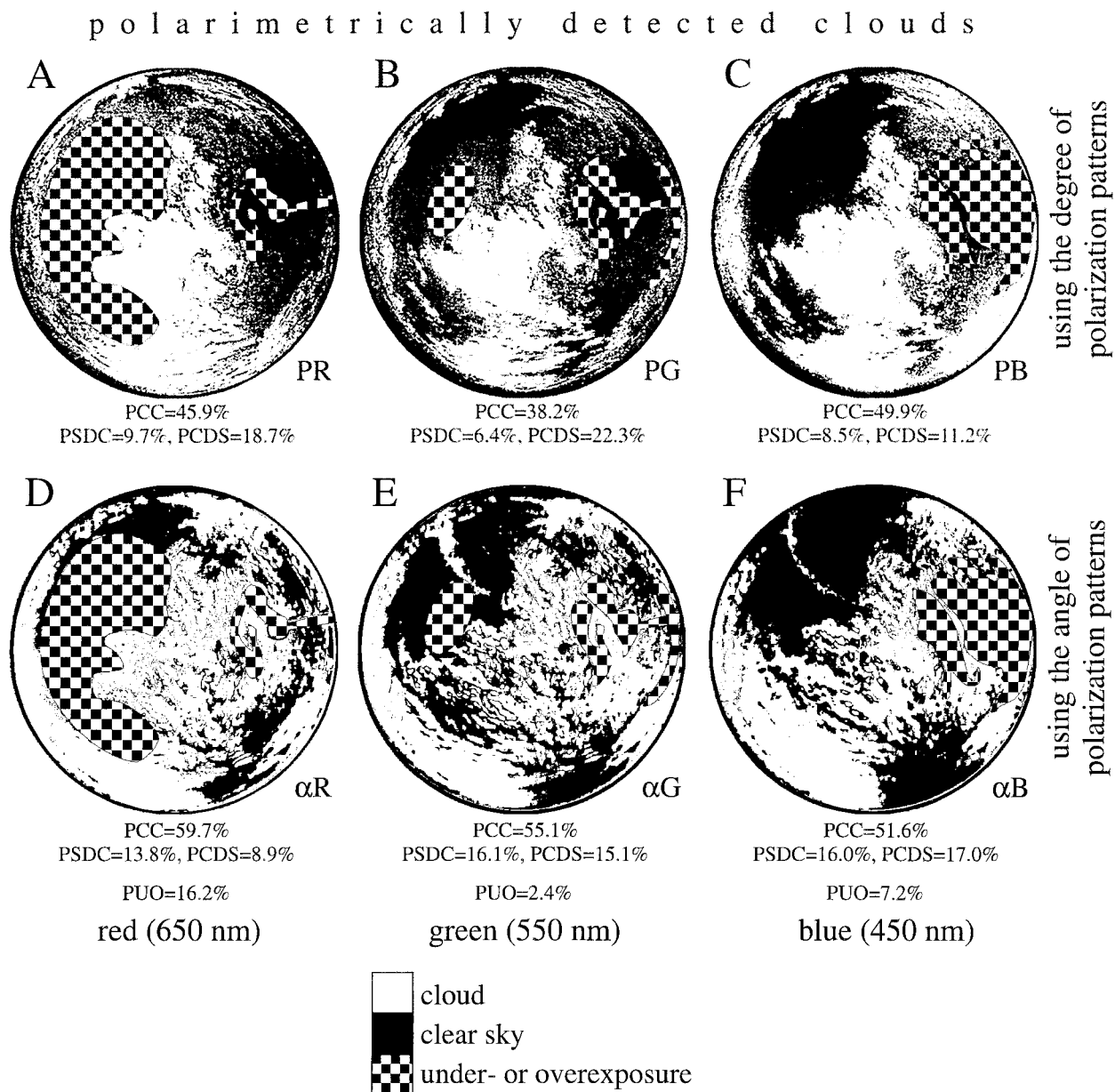
Fig. 10.   Clouds detected polarimetrically in the red (650 nm), green (550 nm), and blue (450 nm) spectral ranges with the degree or angle of polarization patterns in Figs. 7 and 8.   Other conventions as in Fig. 9.

where $Q = R, G, B$.   When we appropriately set their values, certain types of clouds can be reliably detected.

The optimal values of these control parameters are empirically determined in the following way: In the digitized color picture of a given cloudy sky the clouds are visually identified by inspection with the naked eye, and each pixel is marked accordingly.   The resulting cloud pattern serves as control pattern. Changing the value of the control parameter of a given detector, we compare the visually detected control clouds with the clouds recognized by the detector. The numbers of pixels are counted, where (i) there is cloud in the control pattern but the pixel is identified erroneously as clear sky, (ii) there is clear sky in the

control pattern but the pixel is identified erroneously as cloud; (iii) the pixel is identified as cloud, (iv) the pixel is under- or overexposed.

Dividing these numbers by the number of pixels $N = 346207$ of the entire sky, we obtain (i) the proportion PCDS of clouds detected (erroneously) as (clear) sky, (ii) the proportion PSDC of (clear) sky detected (erroneously) as cloud, (iii) the proportion PCC of cloud cover, (iv) the proportion PUO of under- and/or overexposed pixels, (v) the proportion PED = PCDS + PSDC of erroneous detection.   That value of the control parameter of a given detector is considered as optimal $[c^*, p_0^*(Q), \Delta\alpha^*(Q)]$, at which the PED value is minimal (PED*), that is, where the correlation between the pixels of the algorithmically and

map of cloud likelihood

map of authenticity

A

B

number n of cloud identification

0 1 2 3 4 5 6 7 8 9

9
4
2
0

number m of active detectors (authenticity)

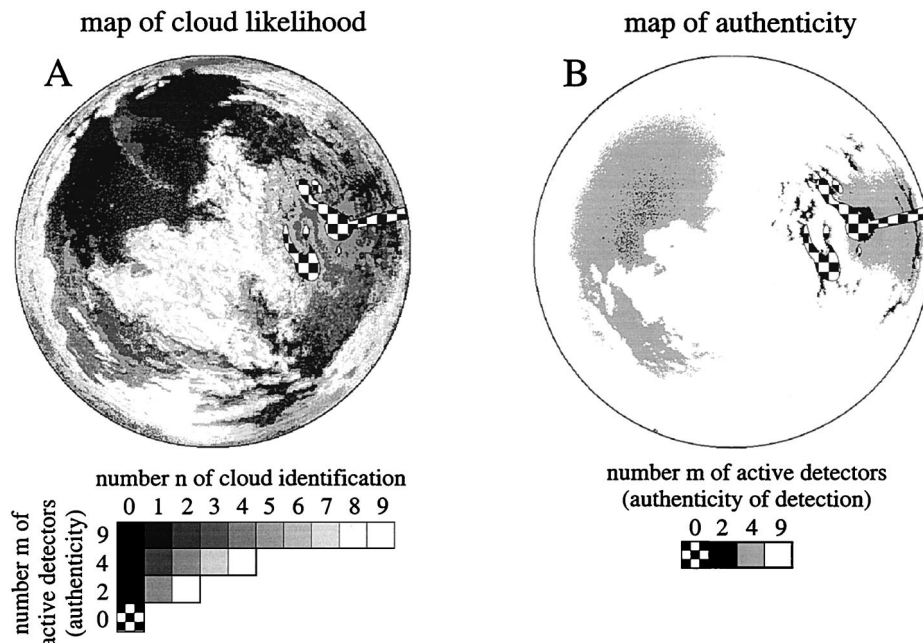number m of active detectors
(authenticity of detection)

0 2 4 9

Fig. 11. (a) Gray-coded map of the number n of cloud identification calculated for the partially cloudy sky in Fig. 9(a), the optical characteristics of which are shown in Fig. 7. (b) Gray-coded map of the number m of active (neither underexposed nor overexposed) detectors calculated for the partially cloudy sky in Fig. 9(a). m is proportional to the authenticity of the (cloud or clear sky) detection. The under- or overexposed sky regions ($m = 0$) as well as the sun occulter in the maps are checkered.

visually detected clouds and clear sky regions is maximal.

1. Radiometric Detection of Colorless Clouds

Detector IRGB functions in the following way: Aside from the reddish orange clouds illuminated by sunset or sunrise glow, or from the very high altitude bluish cirrus clouds, clouds are generally colorless, ranging from dark grey to bright white, independently of their radiance and position in the sky.[14,15] The pixels of such gray clouds on the sky picture possess approximately the same radiances in all three (r, g, b) spectral ranges. Thus if the differences $\Delta I_{b-r} = |I_b - I_r|$ and $\Delta I_{b-g} = |I_b - I_g|$ are less than $\epsilon = c \times I_b$, where c is a control parameter to be chosen appropriately as described above, then detector IRGB assumes that the given pixel belongs to a gray cloud, else to the blue sky. ϵ is the width of the narrow interval, in which the differences between I_r, I_g, and I_b of a given pixel fall if the pixel is colorless enough and thus is detected as cloud. ϵ is proportional to the radiance I_b that is measured in the blue range of the spectrum, due to the blueness of scattered skylight.

2. Polarimetric Detection of Clouds on the Basis of the Degree of Polarization

Detectors PR, PG, and PB function as follows. Apart from 145° from the sun in the sky with water clouds (where rainbow scattering dominates with high degrees of polarization), independently of the wavelength, in a given celestial point the degree of polarization for cloud pixels is lower than that for clear-sky pixels due to diffuse (multiple) scatter-

ing.[14,15] As a first approximation we describe the change of the degree of linear polarization p of skylight versus the angular distance γ from the sun using the single-scattering Rayleigh model, in which $p(\gamma) = p_{\max} \times \sin^2 \gamma/(1 + \cos^2 \gamma)$, $\cos \gamma = \sin \theta_s \sin \theta \cos \phi + \cos \theta_s \cos \theta$, where θ_s is the solar zenith angle, and θ and ϕ are the angular distances of the observed celestial point from the zenith and the solar meridian, respectively (Fig. 5). Detector PQ (Q = R,G,B) assumes that the given pixel positioned at angular distance γ from the sun belongs to a cloud if the degree of polarization p is lower than the threshold $p_{\text{threshold}} = p_0(Q) \times \sin^2 \gamma/(1 + \cos^2 \gamma)$, where $p_0(Q)$ is a control parameter to be chosen appropriately as described above.

3. Polarimetric Detection of Clouds on the Basis of the Angle of Polarization

Under certain meteorological conditions (if parts of the clouds and the airspace between the clouds and the surface of the earth are not directly lit by the sun) in a given celestial point, the angle of polarization α for cloud pixels differs considerably from the angle of polarization $\alpha_{\text{clear sky}}$ for clear sky pixels independently of the wavelength.[8,14] Detector αQ (Q = R,G,B) assumes that the given pixel belongs to a cloud if the difference $|\alpha - \alpha_{\text{clear sky}}|$ is larger than the threshold $\Delta\alpha(Q)$, which is a control parameter to be chosen appropriately as described above. For these decisions we use the angle of polarization patterns of the clear sky (Fig. 8) measured in the R, G, B spectral ranges with the same solar zenith angle as that of the investigated cloudy sky (Fig. 7) as a control. Prior to these decisions the angle of polarization patterns of
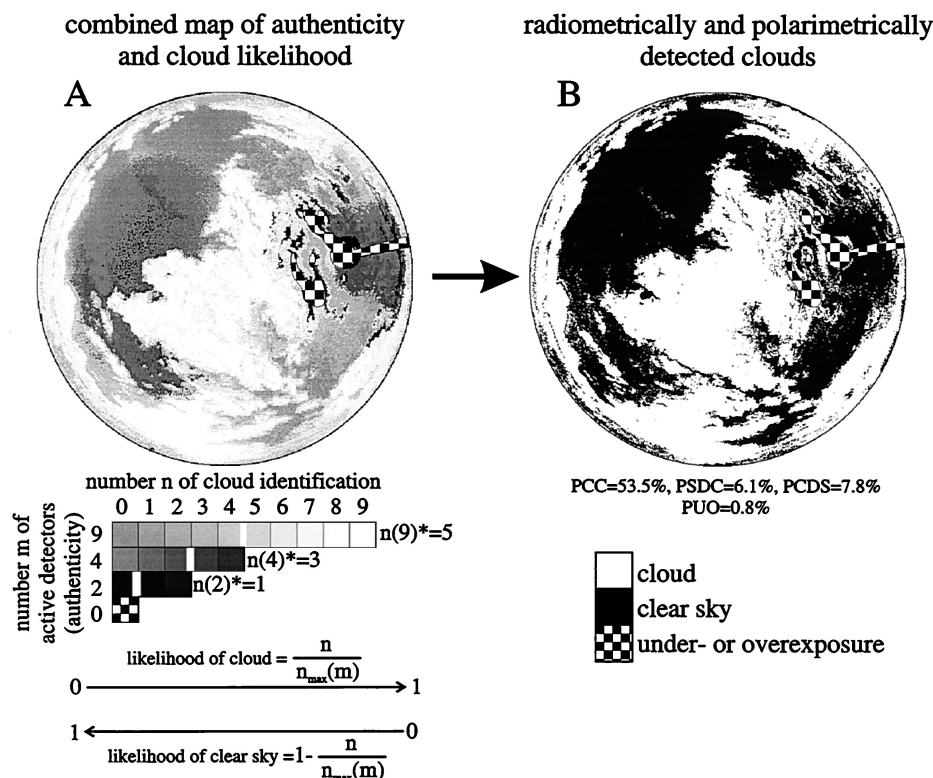
combined map of authenticity and cloud likelihood

radiometrically and polarimetrically detected clouds

A

B

number n of cloud identification

0 1 2 3 4 5 6 7 8 9

number m of active detectors (authenticity)

9

4

2

0

$n(9)^* = 5$

$n(4)^* = 3$

$n(2)^* = 1$

likelihood of cloud $= \dfrac{n}{n_{max}(m)}$

$0 \xrightarrow{\hspace{3cm}} 1$

$1 \xleftarrow{\hspace{3cm}} 0$

likelihood of clear sky $= 1 - \dfrac{n}{n_{max}(m)}$

PCC=53.5%, PSDC=6.1%, PCDS=7.8%
PUO=0.8%

cloud
clear sky
under- or overexposure

Fig. 12. (a) Map combining maps a and b in Fig. 11. At a given value of m, the value of $n/n_{max}(m)$ is the likelihood of cloud, while $1 - n/n_{max}(m)$ is the likelihood of clear sky. (b) Cloudy (white) and clear (black) sky regions detected by the combined (radiometric and polarimetric) algorithm such that pixels with larger or smaller $n(m)$ values than $n(m)^*$ were considered to belong to clouds or clear sky regions, respectively. For $n(2)^* = 1$, $n(4)^* = 3$, and $n(9)^* = 5$ (the positions of which are indicated by white vertical bars in the gray palette) the proportion of erroneous detection PED = PCDS + PSDC is minimal (PED* in Table 1). The under- or overexposed sky regions ($m = 0$) as well as the sun occulter in the maps are checkered.

the corresponding clear and cloudy skies are smoothed by convolution with a two-dimensional rotation-symmetric Gaussian function $G(r) \sim \exp(-r^2/\sigma^2)$ in order to eliminate the inevitable small noise of higher spatial frequencies. The diameter of our circular pictures of the sky was 664 pixels, and the value of parameter σ of the Gaussian filter was 4 pixels.

3. Results

A. Detection of Clouds by Radiometric, Polarimetric, and Combined Algorithms

Figure 7 shows the patterns of the degree and angle of polarization of a sky with fast-moving cumuli measured by our three-lens, three-camera, full-sky imaging polarimeter in simultaneous mode in the red (650 nm), green (550 nm), and blue (450 nm) spectral ranges. In Fig. 8 the corresponding patterns of a clear, cloudless sky are seen with the same solar position as in Fig. 7. The merits and limits of the radiometric, polarimetric, and combined (radiometric and polarimetric) cloud-detection algorithms are demonstrated by these patterns.

Figure 9(a) shows the photograph of the partially cloudy sky, the polarization characteristics of which are represented in Fig. 7. In this subsection we show a possible way that the clouds in Fig. 9(a) can be

detected radiometrically and/or polarimetrically. To test the cloud-detection performance of any algorithm, control patterns would be needed with known, well-defined clouds. Unfortunately, such control cloud patterns are generally not available. Thus the first step of our cloud detection was to construct a relatively good approximation of such a control pattern. Placing trust in the excellent pattern recognition and good brightness and color discrimination ability of the human visual system, we detected and recognized visually the clouds in the color picture of the sky [Fig. 9(a)], which was displayed on the screen of a computer, and those celestial regions were shaded by a mouse-guided paint brush where clouds were seen. Figure 9(b), serving as control cloud pattern, shows the visually detected clouds in white and the clear sky regions in black. The percentage of cloud cover in this control pattern is PCC = 56.1% (= number of visually detected cloud pixels/N, where $N = 346207$ = number of pixels of the full sky).

Figure 9(c) represents the clouds detected radiometrically by the use of the algorithm (detector IRGB) described in Subsection 2.C.1. In Fig. 9(c) regions of the sky are checkered, if their pixels are under- or overexposed in at least one of the three (red, green, blue) spectral ranges in which measurements were performed. In these checkered regions detec-

Algorithm (detector)	Optimal value of the control parameter	Minimum of PED (PED*)
IRGB	$c^* = 0.44$	10.5%
PR	$p_0^*(\text{R}) = 33\%$	28.4%
PG	$p_0^*(\text{G}) = 28\%$	28.7%
PB	$p_0^*(\text{B}) = 33\%$	19.6%
αR	$\Delta\alpha^*(\text{R}) = 7.0°$	22.7%
αG	$\Delta\alpha^*(\text{G}) = 7.0°$	32.5%
αB	$\Delta\alpha^*(\text{B}) = 2.5°$	33.0%

Detection type	Threshold values of $n(m)$
Polarimetric	$n(2)^* = 1$, $n(4)^* = 3$, $n(6)^* = 3$
Combined	$n(2)^* = 1$, $n(4)^* = 3$, $n(9)^* = 5$

[a]Cloudy and clear-sky regions are detected by the polarimetric and combined algorithms such that pixels with larger or smaller $n(m)$ values than $n(m)^*$ are considered to belong to clouds or clear-sky regions, respectively.

tor IRGB is inactive. In Fig. 9(c) the percentage of cloud cover is PCC = 50.7%, the proportion PSDC of clear sky detected erroneously as cloud is 4.5%, the proportion PCDS of clouds detected erroneously as clear sky is 6.0%, and the proportion PUO of under- and/or overexposure is 22.6%. Figures 10(a)–10(f) show the clouds detected polarimetrically in the red (650 nm), green (550 nm), and blue (450 nm) spectral ranges with use of the degree of polarization patterns in Fig. 7 and the angle of polarization patterns in Figs. 7 and 8, respectively. The values of PCC, PSDC, PCDS, and PUO determined by the detectors PR, PG, PB, αR, αG, and αB are indicated below the corresponding cloud patterns in Fig. 10.

The cloud-detection performance of every detector is determined by a control parameter, which is c for detector IRGB, $p_0(\text{Q} = \text{R, G, B})$ for detectors PR, PG, PB and $\Delta\alpha(\text{Q} = \text{R, G, B})$ for detectors αR, αG, αB. The value of a control parameter is optimal if the proportion PED = PCDS + PSDC of erroneous detection is minimal. The graphs PED(c), PED[$p_0(\text{Q})$], PED[$\Delta\alpha(\text{Q})$]–that is, the change of PED as a function of the corresponding control parameters c, $p_0(\text{Q})$, or $\Delta\alpha(\text{Q})$ for detectors IRGB, PR, PG, PB, αR, αG, and αB–possess a definite minimum. The positions of these minima were chosen as the optimal values c^*, $p_0^*(\text{Q})$, $\Delta\alpha^*(\text{Q})$ of the control parameters. Table 1 summarizes the optimal values of the control parameters of the different cloud-detection algorithms (detectors in Figs. 9 and 10).

A detector is inactive at those pixels of the picture of the sky where under- or overexposure occurs. This is the case in the checkered regions in Figs. 9(c) and 10, where there is no information about the real sky conditions. The radiometric detector IRGB actually involves three detectors (IR, IG, and IB), which can function only together. Since detector IRGB is inactive if under- or overexposure occurs in at least one of the three (red, green, blue) spectral ranges, the number m of active (neither underexposed nor overexposed) detectors can be 0, 2, 4, or 9, when the investigated celestial point is under- or overexposed in 3, 2, 1, or 0 spectral ranges, respectively. Thus, the number n of cloud identification can be 0,1, . . . , 8, 9. Figures 11(a) and 11(b) show the gray-coded celestial maps of n and m calculated for the partially

cloudy sky in Fig. 9(a), the optical characteristics of which are shown in Fig. 7. m is proportional to the authenticity (or reliability) of the (cloud or clear-sky) detection. Figure 12(a) shows the map that combines maps A and B of Fig. 11. At a given value of m, the value of $n/n_{\max}(m)$ is the likelihood of cloud, while $1 - n/n_{\max}(m)$ is the likelihood of clear sky.

Figure 12(b) shows the cloudy and clear-sky regions detected by the combined (radiometric and polarimetric) algorithm such that the pixels with larger or smaller $n(m)$ values than $n(m)^*$ were considered to belong to clouds or clear-sky regions, respectively. For $n(m)^*$ the proportion of erroneous detection PED (= PCDS + PSDC) is minimal (PED*). A similar procedure was applied in the case of the polarimetric cloud detection, when only the degree and angle of polarization patterns were used. Table 2 shows the threshold values $n(m)^*$ of the polarimetric and combined cloud-detection algorithms as a function of m.

In Table 3 we compare the lower and upper limits of the proportion of cloud cover determined by the radiometric, polarimetric, and combined (radiometric and polarimetric) cloud-detection algorithms. PCC_{det} is the value of PCC determined by the radiometric [Fig. 9(c)], polarimetric (Fig. 10) and combined [Fig. 12(b)] algorithms. The lower and upper limit of PCC is $\text{PCC}_{\min} = \text{PCC}_{\text{det}} - \text{PSDC}$ and $\text{PCC}_{\max} = \text{PCC}_{\text{det}} + \text{PCDS} + \text{PUO}$, respectively. The real value PCC_{real} of the proportion of cloud cover is between $\text{PCC}_{\min}$ and $\text{PCC}_{\max}$. As an approximate value of PCC_{real} we obtained 56.1% by visual cloud detection [Fig. 9(b)]. The reliability of a cloud detection algorithm is characterized by the difference $\Delta\text{PCC} = \text{PCC}_{\max} - \text{PCC}_{\min}$; the smaller is ΔPCC, the higher is the reliability. We can see in Table 3 that ΔPCC is largest (33.1%) for the radiometric, smaller (20.8%) for the polarimetric and smallest (14.7%) for the combined cloud detection. In the case of the combined cloud detection the interval in which PCC_{real} can be is about the half of that obtained for the radiometric cloud detection. This demonstrates well that in the investigated case the combined algorithm can detect clouds more reliably than the exclusively radiometric or the purely polarimetric algorithm can alone.

Table 3. Numerical Values of the Proportion of Cloud Cover Detected by the Radiometric, Polarimetric, and Combined (Radiometric and Polarimetric) Cloud-Detection Algorithms[a]

Detection type	$PCC_{det} - PSDC =$	$PCC_{min} \leq PCC_{real} \leq PCC_{max}$	$= PCC_{det} + PCDS + PUO$	$PCC_{max} - PCC_{min}$
Radiometric	$50.7\% - 4.5\% =$	$46.2\% \leq 56.1\% \leq 79.3\%$	$=50.7\% + 6.0\% + 22.6\%$	33.1%
Polarimetric	$59.4\% - 12.1\% =$	$47.3\% \leq 56.1\% \leq 68.1\%$	$=59.4\% + 7.9\% + 0.8\%$	20.8%
Combined	$53.5\% - 6.1\% =$	$47.4\% \leq 56.1\% \leq 62.1\%$	$=53.5\% + 7.8\% + 0.8\%$	14.7%

[a]PUO, proportion of under- and overexposure; PED, proportion of erroneous detection; PCDS, proportion of clouds detected (erroneously) as (clear) sky; PSDC, proportion of (clear) sky detected (erroneously) as cloud; PCC, proportion of cloud cover; PCC_{real}, real value of PCC; PCC_{det}, value of PCC detected by a given algorithm; PCC_{min}, lower limit of PCC; PCC_{max}, upper limit of PCC. $PED = PCDS + PSDC$. The number of pixels of the entire sky is $N = 346207$, to which all percentage values are related.

4. Discussion

A. Advantages of Three-Lens, Three-Camera, Full-Sky Imaging Polarimeters over One-Lens, One-Camera Polarimeters

Our three-lens, three-camera, full-sky imaging polarimeter combines some advantageous characteristics of the earlier 180° imaging polarimeters: (1) It takes the three polarization pictures of the entire sky simultaneously like the instrument of North and Duggin.[1] (2) Its setting up and disassembly are easy and quick as with the polarimeters of Voss and Liu,[2] Liu and Voss,[3] Gál et al.[4–6] and Pomozi et al.[7,8] (3) It is portable, not being dependent on a power supply of 220 V or 110 V; it needs neither thermoelectrical cooling nor connection with a computer, and its transfer and transport are as convenient as the equipment of Gál et al.[4–6] and Pomozi et al.[7,8] Modifying appropriately the design, we can adapt our three-lens, three-camera 180° field-of-view imaging polarimeter to underwater measurements too, like the submersible videopolarimeter designed by Shashar et al.[16]

With use of an imaging polarimeter in sequential mode, the consequences of the displacement of fast moving clouds would be the introduction of such motion artefacts, which would falsify the real values of the degree and angle of polarization as well as of radiance within and around moving clouds in the sky after computer evaluation. Since the filtering of these artefacts would be extremely difficult, they make impossible the reliable detection of clouds in the sky. These artefacts can be eliminated only through simultaneous exposure. This is the major advantage of a three-lens, three-camera imaging polarimeter over a one-lens, one-camera polarimeter.

At sunset or sunrise the radiance of skylight decreases or increases rapidly in time.[14,15] After sunset and prior to sunrise the sky radiance is so low that the necessary time of exposure can reach 15–30 seconds even if the photoemulsion (detector) is highly sensitive (1600 ASA for Kodak EPH color reversal film, for example). In this case the time needed to take the three polarization pictures of the sky sequentially is at least 3×15–$30 = 45$–90 seconds, a period during which the change of the skylight radiance is considerable, also, changes in the scene may occur owing to the movement of clouds or other aerial objects (e.g., birds or airplanes). Thus the sequential exposure introduces inevitable errors in the degree and angle of polarization patterns of skylight owing to this rapid temporal change of the sky radiance. This can be eliminated only by simultaneous exposure.

B. Limits of Three-Lens, Three-Camera, Full-Sky Imaging Polarimeters

Our polarimeter uses normal photographic cameras with roll films. Digital cameras with appropriate 180° fish-eye lenses could be used as well. In the latter case the development of the color reversal films as well as the digitization of the color slides are spared.

The use of three photographic cameras (of the same type) with three roll films (of the same lot) and three linear polarizers (of the same type) involves the influence of inevitable sources of errors caused by the possible slight differences between (i) the emulsions, (ii) the polarizers, (iii) the processing of the films, and (iv) the shutter-controlling signals and the accuracy of the exposure timing of the cameras. With the use of digital cameras, only source (iii) can be eliminated, because in this case there are small differences between the CCD arrays, the polarizers, and the working of the cameras.

Other limitations of our system are that a large number of images would be difficult to handle in an automated fashion, because of the need for (i) the development of the roll films, (ii) the framing of the developed color dia positives, and (iii) the digitization of the dia slides. Large numbers of images can be handled automatically only with the use of a polarimeter that is based on three digital cameras. In the future we plan to replace the roll-film cameras with digital ones.

We admit that occluding the sun by a screening plate at the end of a rod held by an assistant (Fig. 4) is not elegant, and in violent wind the handling of the sun occulter is a difficult task. However, it is practical for field work and the simplest way to hinder the direct solar radiation of all three fish-eye lenses that are arranged along the horizontal guide of about 50-cm length (Fig. 1). To eliminate the multiple internal reflections of direct sunlight from the numerous refracting surfaces within the fish-eye lenses, all three lenses have to be in the shadow of the screening plate, which explains its dimensions (diameter ≥ 0.5 m).

Our three-lens, three-camera, 180° field-of-view

imaging polarimeter in its present layout can be used not only to record the polarization pattern of the full sky but also to measure the polarization characteristics of any aerial and terrestrial scenes (e.g., landscapes, water and ground surfaces, or vegetation) if the object is not too close to the polarimeter. In the case of near objects the spatial disparity–due to the difference between the angles of view of the three fish-eye lenses, which is the basis of stereo photography,[17] for example–may result in difficulties that could be hard to overcome in the evaluation of the three polarization pictures. The same problem occurs with the sun occulter if it is positioned relatively close to the polarimeter (Fig. 4). Thus in the evaluated patterns three slightly displaced contours of the sun occulter are visible, the union of which is covered by an appropriate mask (Figs. 7–12).

The layout of our three-lens, three-camera, full-sky imaging polarimeter is not ideal for the measurement of the reflection-polarization characteristics of a water surface, for example, because the object is generally too close to the polarimeter (it would be difficult to ensure the appropriately high suspension of the polarimeter over the water). For this purpose a one-camera 180° field-of-view imaging polarimeter used by Gál et al.,[4] for instance, is more advantageous, if the water surface is flat. The reflection-polarization patterns of rippled water surfaces, however, could be measured only by three-lens, three-camera imaging polarimeters in simultaneous recording mode.

Since the radiance of skylight changes by several orders as the direction of view changes from the sky region next to the sun towards 90° from the sun, it is impossible to avoid the under- or overexposure of the detector of a full-sky imaging polarimeter in certain sky regions. Since the scattered skylight is the brightest (darkest) in the blue (red) range of the spectrum, the overexposed (underexposed) celestial areas are the greatest in the blue (red) spectral range (Figs. 7–10). The area of overexposed or underexposed sky regions could be reduced through a decrease or increase in the time of exposure and/or the aperture of the objective, but this would result in the increase or decrease of the underexposed or overexposed regions, respectively. Moreover, if the clouds move rapidly in the sky, it is impossible to take photographs with different exposures and/or apertures from the same cloudy sky.

If it is not just the brightest sky regions with very low degrees of polarization–in the vicinity of the sun and the Babinet, Brewster neutral points–that have to be studied, the overexposure does not matter, since the detector is overexposed anyway in the immediate vicinity of the sun (Figs. 7–10). If on the contrary, the regions of the sky with the highest degrees of polarization have to be investigated, underexposure is a real problem, because it always occurs at about 90° from the sun, where the sky is most polarized and least bright (Figs. 7–10). If possible, we take the three polarization photographs of a given sky generally with two or three different times of exposure, and after their evaluation we select the triplet with the

minimal proportion of the union of the under- and overexposed sky regions.

A polarimeter using a 16-bit CCD array has a wider dynamic range than the eight-bit photoemulsion–digitizer technique used in our system that ends up with more under- or overexposed pixels. In the future the dynamic range of our polarimeter can be extended to 16 or 32 bits by the use of other photoemulsions, scanners, or digital cameras.

Full-sky imaging polarimeters use generally 180° field-of-view fish-eye lenses,[2–8] which include numerous optical elements made of ultraviolet-absorbing glasses. Thus skylight polarization in the ultraviolet spectral range cannot be measured by these lenses. For polarimetric measurements in this spectral range either UV-transmitting fish-eye lenses (composed of quartz) or UV-reflecting hemispherical mirrors–as used by North and Duggin[1] or the TSI-880 Total Sky Imager[9]–are needed.

C. Comparison between Combined and Exclusively Radiometric or Polarimetric Cloud-Detection Algorithms

Earlier in this paper we presented a possible way (Figs. 9–12; Tables 1 and 2) to improve an algorithm of radiometric cloud detection (IRGB) through the use of additional information, namely the degree and angle of polarization patterns (Figs. 7 and 8) of the sky measured by ground-based full-sky imaging polarimetry in the red, green, and blue spectral ranges. As also demonstrated by Table 3, the combined radiometric and polarimetric algorithm is able to detect the clouds with much more reliability than the radiometric algorithm alone. The reason for this, of course, is that the combined algorithm actually relies upon seven detectors (subalgorithms IRGB, PR, PG, PB, αR, αG, and αB), while the purely radiometric algorithm uses only one detector (IRGB). If detector IRGB is inactive because of under- or overexposure, the sky conditions (cloudy or clear) cannot be determined radiometrically. Thus the higher the proportion PUO of under- and/or overexposure in the color picture of the sky is, the lower the reliability of the radiometric cloud detection is (that is, the wider the interval is in which the real proportion PCC_{real} of cloud cover may be). In the case of the combined algorithm the deficiency of detector IRGB due to under- or overexposure does not induce automatically a high net PUO value if several other detectors are still active. Hence, the power of the combined cloud detection algorithm is ensured by the fact that the information contributed by the radiometric subalgorithm (subdetector IRGB) to the final decision (cloud or clear sky) is only one-third by weight.

Table 3 also shows that the polarimetric algorithm is more reliable than the radiometric one. The reason for this is again that the former is based on the use of twice as many detectors as the latter. It can be also read from Table 3 that formally the higher reliability of the combined and the polarimetric cloud detection in comparison with the authenticity of the radiometric cloud detection is mainly due to the much

smaller PUO values. Thus the advantage of the combined algorithm is expected to decrease with the decrease of the area of the under- or overexposed sky regions. However, as we have already pointed out in subsection 4.C, some amount of under- or overexposure is generally unavoidable in full-sky polarimetric measurements, even for an increased dynamic range of the detectors of the polarimeter, so the lack of polarization information in the radiometric cloud detection cannot be compensated fully by the enhancement of the dynamic range of the camera.

Our combined cloud-detection algorithm is based on the assumption that perfect radiometric and polarimetric detectors (i.e., detectors that are not affected by measurement errors or restricted in dynamical range) would detect identical cloud patterns. However, since detectors IRGB, PR, PG, PB, αR, αG, and αB measure different optical parameters, the measurement results will not always agree. For example, a radiometrically subvisible cirrus cloud is not detectable by detector IRGB, but might produce a clear signature in the observations by detectors PR, PG, PB or αR, αG, αB. Therefore in such cases the combination of radiometric and polarimetric detection methods does not give a more reliable estimate of cloud pattern and percentage of cloud cover in comparison with the exclusively polarimetric detection methods. The wide range of PCC–varying between 38.2% [Fig. 10(b)] and 59.7% [Fig. 10(d)]–may not be entirely due to erroneous detection but might be interpreted as an indication that the assumption $PCC(I) = PCC(p) = PCC(\alpha)$ is not always valid. Thus in the future we plan to investigate the question of which meteorological situations will the combined algorithm give a more reliable estimate of cloud cover as compared with exclusively polarimetric cloud detection algorithms.

D. Improvement Possibilities of the Combined Radiometric and Polarimetric Cloud-Detection Algorithm

A reliable cloud-detection algorithm is able to recognize the pattern of clouds in the sky, from which the numerical values of several parameters (e.g., PCC, PSDC, PCDS, PUO) of the cloudy sky can be calculated. In meteorology and atmospherical physics usually only the measured value of the proportion PCC of cloud cover is needed as one of the most important input data of the climate or radiative transfer models, for example. The PCC values given in Figs. 9–12 and Table 3 are the raw percentages of cloud cover in the picture of the sky as photographed by the imaging polarimeter. Like the radiometric cloud detection software used by the TSI-880 Total Sky Imager,[9] we did not take into consideration the curvature of the sky and the distorted perspective in the calculation of the fractional cloud cover; that is, all pixels were weighted equally. With use of appropriate geometric transformations (taking into account the curvature of the sky dome as well as the perspective), the real cloud-cover fraction can be calculated from the raw PCC value obtained by our combined cloud-detection algorithm. The derivation

and discussion of these transformations is out of the scope of this work.

As we have seen above, one decisive step of our combined radiometric and polarimetric cloud-detection algorithm is the determination of the optimal values $[c^{*}, p_{0}^{*}(Q = R, G, B), \Delta\alpha^{*}(Q = R, G, B)]$ of the control parameters $[c, p_{0}(Q), \Delta\alpha(Q)]$ of detectors IRGB, PR, PG, PB, αR, αG, and αB. In the future we plan to produce additional control-cloud patterns for a variety of cloudy skies in order to study how the optimal values of the control parameters vary as a function of the sky condition. Our combined cloud-detection algorithm will function reliably only in cases when the averages of the optimal values of the control parameters show relatively small standard deviations.

There are numerous different cloud types, and we expect to find different optimal values for different kinds of clouds. Also, optimal values should more or less depend on the position of the clouds in the sky and on the solar zenith angle. One can mention the sunset sky, for example: At sunset the clouds near the setting sun and the rising anti-sun reflect the reddish sunset glow. Another example is the case of the high-altitude cirrus clouds; they show up in the sky usually rather bluish owing to the Rayleigh scattering of sunlight in the air column beneath them. The optimal values of the control parameters of the algorithms that can reliably detect these reddish-orange or bluish clouds should differ from those of algorithms that can recognize colorless clouds. By determining the optimal values of the control parameters for different cloud types, we can fine tune combined cloud detection algorithms to meet special requirements or to adapt to local weather characteristics. Furthermore, in order to be usable in the future as an automatic full-sky imaging system our cloud detection method would require additional algorithms that perform cloud classification and determination of whether the detected clouds may be composed of water droplets or ice crystals similarly to the algorithm used by the POLDER spaceborne imaging polarimeter.[18] The realization of the latter and the proper adjustment of the control parameters are the tasks of future studies.

In our combined radiometric and polarimetric algorithm, detectors PR, PG, and PB assume that a pixel positioned at an angular distance γ from the sun belongs to a cloud if the degree of polarization p is lower than the threshold value $p_{\text{threshold}} = p_{0}(Q) \times \sin^{2}\gamma/(1 + \cos^{2}\gamma)$, which was calculated on the basis of the single-scattering Rayleigh model. In the case of water clouds positioned at about 145° from the sun this assumption is not true because of the high p values, owing to the rainbow scattering. In an improved version of our algorithm this effect can be considered and $p_{\text{threshold}}$ can be calculated on the basis of a more sophisticated atmospheric scattering model,[15] which also takes into account multiple scattering, for example.

In the combined algorithm the detectors αR, αG, and αB assume that a pixel with angle of polarization α belongs to a cloud if $|\alpha - \alpha_{\text{clear sky}}|$ is larger than the

threshold value $\Delta\alpha(Q = R, G, B)$. Detectors αR, αG, and αB do not function reliably if the angle of polarization α_{cloud} of clouds does not differ considerably from the corresponding angle of polarization $\alpha_{clear\ sky}$ of the clear sky. This will be the case if the air columns beneath clouds and parts of clouds are lit by direct sunlight (i) obliquely from above (for smaller solar zenith angles), (ii) from the side (as with white cumuli), or (iii) from below (as sometimes at sunset or sunrise). The implication here is that the Earth's surface has to be in sunlight but not at the position of the observer. In other words, under these illumination conditions the clear-sky angle of polarization pattern more or less continues underneath clouds; that is, α_{cloud} is approximately the same as $\alpha_{clear\ sky}$.[8,14] Apart from heavy overcast with multiple cloud layers, such conditions occur frequently if the sky is partly cloudy.

Our cloud-detection algorithms presented in this work are based on decisions (cloud or clear sky) that use the optical parameters measured in independent pixels of the sky picture; they do not take into consideration optical information from neighboring pixels. Another possible way to improve our cloud-detection method would be the addition of common pattern-recognition algorithms that use cluster analysis and edge detection. Using different weight (e.g. Gaussian or "Mexican hat") functions, these algorithms will take into account the information from the neighborhood of every pixel in the sky image and will analyze the gradients of the patterns of the radiance as well as the degree and angle of polarization of the sky.

5. Conclusions

Although three different kinds of full-sky imaging polarimeters working in sequential mode have been designed in the past and various aspects of the polarization distribution in the sunlit atmosphere have been studied with them, ground-based simultaneous measurements of the polarization pattern over the whole celestial hemisphere were not previously possible. In this paper we reported on a three-lens, three-camera, full-sky imaging polarimeter, with which the three polarization pictures of the sky can be taken simultaneously. After chemical development, scanning digitization, and computer evaluation of these pictures, the patterns of the radiance, degree of linear polarization, and angle of polarization of the entire sky in the red (650 nm), green (550 nm), and blue (450 nm) spectral ranges are obtained and visualized in high-resolution color or gray-coded image (map) format.

After appropriate modification, our polarimeter also can be adapted to underwater measurements. The major advantage of our polarimeter is that it can be used even if rapid temporal changes occur in the sky owing to moving clouds and other aerial objects, rapid change of the low skylight radiance after sunset and prior to sunrise, or the movement or rocking of the polarimeter's platform. The ability of our polarimeter to provide polarization patterns has great potential for application in atmospheric optics as well as radiative-transfer problems in the Earth-ocean system because data can be collected simultaneously, thus changes in the atmosphere during measurement can be neglected.

As a possible application of our polarimeter, we presented a combined radiometric and polarimetric algorithm that performs the ground-based detection of clouds more efficiently and reliably than an exclusively radiometric cloud-detection algorithm. We demonstrated a possible way to use the additional information of the degree and angle of polarization patterns of cloudy skies. In the future, this or similar improved polarimetric algorithms can accomplish cloud detection with ground-based automatic instruments that will be a new generation of the presently existing ground-based automated total-sky imagers that use exclusively radiometric algorithms for cloud detection.

References

1. J. A. North and M. J. Duggin, "Stokes vector imaging of the polarized sky-dome," Appl. Opt. **36,** 723–730 (1997).
2. K. J. Voss and Y. Liu, "Polarized radiance distribution measurements of skylight. I. System description and characterization," Appl. Opt. **36,** 6083–6094 (1997).
3. Y. Liu and K. J. Voss, "Polarized radiance distribution measurements of skylight. II. Experiment and data," Appl. Opt. **36,** 8753–8764 (1997).
4. J. Gál, G. Horváth, and V. B. Meyer-Rochow, "Measurement of the reflection-polarization pattern of the flat water surface under a clear sky at sunset," Remote Sens. Environ. **76,** 103–111 (2001).
5. J. Gál, G. Horváth, V. B. Meyer-Rochow, and R. Wehner, "Polarization patterns of the summer sky and its neutral points measured by full-sky imaging polarimetry in Finnish Lapland north of the Arctic Circle," Proc. R. Soc. Lond. Ser. A **457,** 1385–1399 (2001).
6. J. Gál, G. Horváth, A. Barta, and R. Wehner, "Polarization of the moonlit clear night sky measured by full-sky imaging polarimetry at full moon: comparison of the polarization of moonlit and sunlit skies," J. Geophys. Res. D **106,** 22647–22653 (2001).
7. I. Pomozi, J. Gál, G. Horváth, and R. Wehner, "Fine structure of the celestial polarization pattern and its temporal change during the total solar eclipse of 11 August 1999," Remote Sens. Environ. **76,** 181–201 (2001).
8. I. Pomozi, G. Horváth, and R. Wehner, "How the clear-sky angle of polarization pattern continues underneath clouds: full-sky measurements and implications for animal orientation," J. Exp. Biol. **204,** 2933–2942 (2001).
9. Description of the TSI-880 Total Sky Imager, Yankee Environmental Systems, Inc., Airport Industrial Park, 101 Industrial Blvd., Turners Falls, Mass. 01376; http://www.yesinc.com; e-mail, info@yesinc.com.

10. R. W. Saunders, "An automated scheme for the removal of cloud contamination from AVHRR radiances over western Europe," Int. J. Remote Sens. **7,** 867–886 (1986).

11. R. W. Saunders and K. T. Kriebel, "An improved method for detecting clear sky and cloudy radiances from AVHRR data," Int. J. Remote Sens. **9,** 123–150 (1988).

12. M. Derrien, B. Farki, L. Harang, H. LeGléau, A. Noyalet, D. Pochic, and A. Sairouni, "Automatic cloud detection applied to NOAA-11/AVHRR imagery," Remote Sens. Environ. **46,** 246–267 (1993).

13. HNP'B, Polaroid Europe Ltd., London, England, http://www.polaroid.com.

14. G. P. Können, *Polarized Light in Nature* (Cambridge U. Press, Cambridge, 1985).

15. K. L. Coulson, *Polarization and Intensity of Light in the Atmosphere* (A. Deepak, Hampton, Va., 1988).

16. N. Shashar, T. W. Cronin, G. Johnson and L. B. Wolff, "Designs for submersible imaging polarimeters," *Ultraviolet Radiation and Coral Reefs*, D. Gulko and P. L. Jokiel, eds., HIMB Tech. Report **41,** 213–218 (1996).

17. F. Mizera, B. Bernáth, G. Kriska, and G. Horváth, "Stereo videopolarimetry: measuring and visualizing polarization patterns in three dimensions," J. Imaging Sci. Technol. **45,** 393–399 (2001).

18. P. Goloub, J. L. Deuzé, M. Herman, and Y. Fouquart, "Analysis of the POLDER polarization measurements performed over cloud covers," IEEE Trans. Geosci. Remote Sens. **32,** 78–88 (1994).